ELSEVIER

Tectonophysics 321 (2000) 407–427

TECTONOPHYSICS

www.elsevier.com/locate/tecto

The Pali Aike Volcanic Field, Patagonia: slab-window magmatism near the tip of South America

Massimo D'Orazio [a,*], Samuele Agostini [a], Francesco Mazzarini [b], Fabrizio Innocenti [a], Piero Manetti [c], Miguel J. Haller [d], Alfredo Lahsen [e]

[a] *Dipartimento di Scienze della Terra, Università di Pisa, via S. Maria, 53, 56126 Pisa, Italy*
[b] *Centro di Studio per la Geologia Strutturale e Dinamica dell'Appennino, C.N.R., via S. Maria, 53, 56126 Pisa, Italy*
[c] *Dipartimento di Scienze della Terra, Università di Firenze, via G. La Pira, 4, 50121 Firenze, Italy*
[d] *Universidad Nacional de la Patagonia San Juan Bosco, CENPAT-CONICET, Puerto Madryn, Argentina*
[e] *Departamento de Geologia, Facultad de Ciencias Fisicas y Matematicas, Universidad de Chile, Santiago, Chile*

Received 26 July 1999; accepted for publication 28 February 2000

Abstract

The Pali Aike Volcanic Field (PAVF) represents the southernmost occurrence of the Cenozoic back-arc Patagonian Plateau Lavas. Its activity (Pliocene–Recent) started forming tabular lavas followed by the growth of about 470 essentially monogenetic volcanic centers (tuff-rings, maars, spatter and scoria cones). Azimuths of cone alignment, cone elongation and morphologic lineations show prevailing ENE–WSW and NW–SE trends. Erupted products consist mainly of alkaline basalt and basanite, with minor olivine basalt. PAVF rocks are quite primitive in composition (average Mg# = 66, Ni = 220 ppm and Cr = 313 ppm) with relatively high TiO_2 (average 3.0 wt.%). Ultramafic garnet- and/or spinel-bearing xenoliths are found within PAVF volcanics. Chondrite-normalized REE patterns are significantly LREE-enriched and almost rectilinear [$(La/Yb)_N = 10.9–21.0$]. Primordial mantle-normalized distributions of incompatible trace elements, as well as Sr and Nd isotope ratios ($^{87}Sr/^{86}Sr = 0.70317–0.70339$, $^{143}Nd/^{144}Nd = 0.51290–0.51294$), show values typical of intra-plate basalts, despite the fact that these rocks occur only 200 km east of the Andean Cordillera. Primary magmas were generated from a fertile garnet-bearing asthenospheric source at $P = 1.9–2.9$ GPa and $T = 1420–1470$°C.

The data suggest a geodynamic model that implies sub-slab asthenosphere flow through a slab window, which started opening below this sector of South America 14 m.y. ago as a consequence of the collision of the Chile Ridge with the Chile Trench. The trailing edge of the Nazca Plate crossed below the Pali Aike area at 9–10 Ma, that is 6–5 m.y. before the onset of the volcanic activity. We hypothesize that this time delay resulted from changes in the kinematics of the South America–Scotia transform plate boundary which only allowed the Pali Aike magmas to rise after about 4 m.y.

Keywords: geodynamics; mafic magmas; Neogene; Patagonia; petrology; slab window

* Corresponding author. Tel.: +39-050-847209; fax: +39-050-500932.
E-mail address: dorazio@dst.unipi.it (M. D'Orazio)

0040-1951/00/$ - see front matter
PII: S0040-1951(00)00082-2

1. Introduction

The petrogenesis, structural setting and geodynamic significance of continental alkaline basaltic magmas erupted close to destructive plate margins are topics of great interest in igneous petrogenesis (e.g. Hole et al., 1995). It is now generally established that the generation of these magmas, often bearing OIB-type or MORB-type geochemical and isotopic signatures, can occur where pristine asthenospheric material replaces, to various extents, or interacts with, mantle domains previously modified by subduction processes. Several mechanisms have been proposed to explain the replacement of the mantle wedge above a subducting slab with upwelling unmodified asthenospheric material. Those most accepted include: (1) slab window opening (Dickinson and Snyder, 1979); (2) slab roll-back (Furlong et al., 1982); and (3) slab-induced asthenospheric convection and upwelling (Toksöz and Bird, 1977). The slab window model is currently the most accepted mechanism for explaining the renewal of supra-slab asthenospheric mantle in regions where ridge-trench collision occurs (Thorkelson, 1996). Examples of alkaline magmatism related to slab window opening can be found along the entire eastern margin of the Pacific Ocean: British Columbia (Bevier, 1983), SW California (Johnson and O'Neill, 1984), Baja California (Saunders et al., 1987), Costa Rica–Panama (Johnston and Thorkelson, 1997), Patagonia (Ramos and Kay, 1992) and Antarctic Peninsula (Hole et al., 1991).

In Patagonia, several Cenozoic plateau lavas, both alkaline and tholeiitic in composition, crop out in a back-arc position. Their origin was linked either to slab window opening related to the subduction of the Nazca (Farallon), Aluk and Antarctic oceanic plates beneath South America (Ramos and Kay, 1992; Gorring et al., 1997), or to the slab-induced thermal and mechanical perturbation of the lower lithospheric and/or asthenospheric mantle (Stern et al., 1990).

The Pali Aike Volcanic Field (PAVF) is the southernmost of the Late Miocene to Recent volcanic exposures occurring in southern Patagonia between 46.5° S (latitude of the Chile Triple Junction, CTJ) and 52° S (Fig. 1). It covers about 4500 km^2 above the Jurassic–Miocene Magallanes Basin, about 400 km north-east of the modern Chile Trench and 220 km north of the conservative boundary between Scotia and South American Plates (Skewes and Stern, 1979; Corbella et al., 1996; Corbella, 1999a). For its peculiar geological setting, close to two distinctly different plate boundaries, the geochemical, petrological and structural investigation of the PAVF has a primary importance for constraining the evolutionary model of southernmost South America, and for elucidating the significance of continental alkaline basaltic magmas erupted in a back-arc position.

2. Geological framework

The Cenozoic geodynamic evolution of southernmost South America resulted mainly from: (1) convergence of the Nazca and Antarctic Plates beneath the South American Plate and (2) transcurrent movements along the boundary between the Scotia and South American Plates.

Plate subduction led to the collision of segments of the Chile Ridge with the Chile Trench. This ridge-trench collision process began west of Tierra del Fuego at about 14 Ma (Cande and Leslie, 1986) with the development of the triple junction between the South American, Nazca and Antarctic Plates. The CTJ has since migrated northward to its present position (~46.5° S) close to the Taitao Peninsula (Cande and Leslie, 1986; Forsythe et al., 1986). This ridge–trench interaction is considered to be responsible for some peculiar geological features, such as the volcanic gap between the Southern Volcanic Zone and the Austral Volcanic Zone of the Andean Cordillera (Futa and Stern, 1988), the Neogene uplift of this sector of the Andes, and the formation of the Patagonian fold-thrust belt (Ramos, 1989).

Transcurrent movement along the northern margin of the Scotia Plate strongly deformed the southernmost tip of South America, forming the Magallanes and Deseado fault zones (Klepeis, 1994). The complex plate boundary configuration resulted in the presence of distinct tectonic provinces in the area. The easternmost part of the continent forms the relatively undeformed

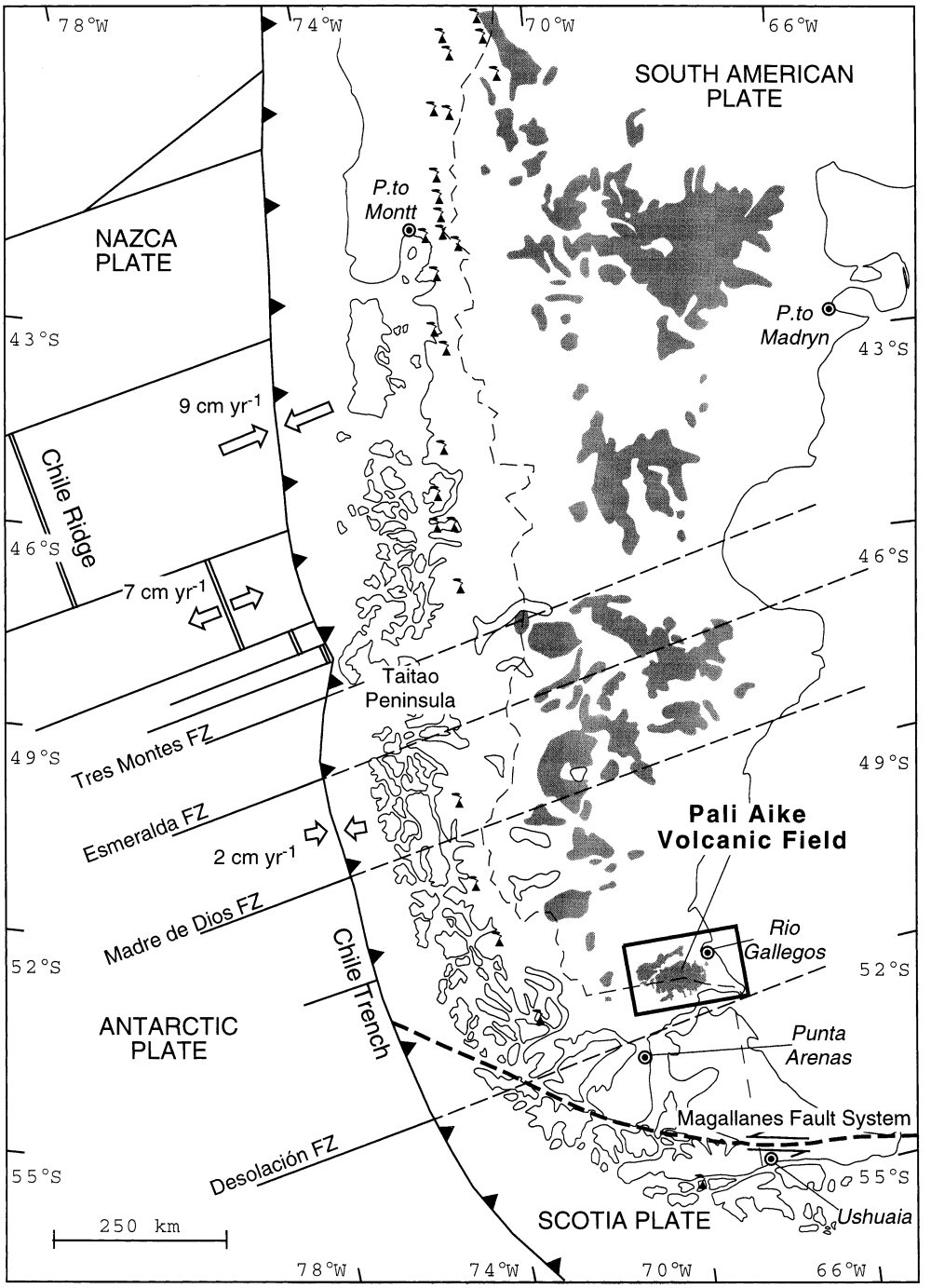

Fig. 1. Schematic geotectonic setting of southern South America and adjacent Pacific Ocean. In the sketch are shown: (1) fracture zones (FZ) of the oceanic Nazca and Antarctic Plates; (2) Chile Ridge; (3) Chile Trench; (4) the main active volcanoes of the Andean Cordillera (filled triangles); (5) Cenozoic Patagonian Plateau lavas (grayed areas); (6) Magallanes Fault System. Redrawn after Forsythe and Prior (1992). Relative motion between plates are form model NUVEL-1 of Gripp and Gordon (1990). Boxed area encloses the studied zone.

Magallanes foreland, west of that is the Cretaceous–Tertiary Magallanes fold-thrust belt, and further west is the Mesozoic to Recent magmatic arc. Slivers of the metamorphic core of Cordillera Darwin and of the Jurassic–Cretaceous Rocas Verdes marginal basin locally intervene between the magmatic arc and the foreland fold-thrust belt (Klepeis, 1994).

Extensive plateau basaltic lavas were erupted in southern Patagonia during the Neogene in a back-arc position. PAVF volcanics were erupted onto the thick sequence of siliciclastic and pelitic sediments of the Magallanes Basin (Winslow, 1982), which represents the filling of the Austral Patagonian rift, the southernmost of a series of NW–SE continental rifts that developed since Late Triassic time due to extensional tectonism linked to the Gondwana break-up (Urien et al., 1995; Corbella et al., 1996). The youngest deposits of the Magallanes Basin are Late Miocene–Holocene fluvial sediments with intercalated pyroclastic materials and glacial sediments (Mercer, 1976; Clapperton, 1983).

3. Geology of Pali Aike Volcanic Field

The volcanic succession of PAVF starts with the effusion of extensive tabular lava flows, locally reaching, as in the northwestern side of the volcanic field, an exposed thickness of more than 120 m (canyon of Rio Gallegos River). This sequence exhibits a planar plateau-like morphology. Steep walls of the main river valleys allow observations of rare remnants of scoria cones, volcanic ramparts, dikes and sills within the sequence.

More than 450, mainly monogenetic, volcanic centers formed above the basal sequence. These include tuff-rings, maars, spatter and scoria cones; the latter two sometimes produced blocky or aa lava flows. Monogenetic centers showing varying degrees of morphological dissection are spread throughout the volcanic field at elevations between 100 and 180 m; sometimes, they are reduced to scarce annular ramparts of welded scoriae representing the innermost portion of deeply eroded cones, occasionally filled by eolian deposits. Cones with well-preserved morphology and not covered by soil, hence of youngest age, occur only in the southeastern area of the volcanic field.

A total of about 30 K–Ar and $^{40}Ar/^{39}Ar$ isotopic datings of Pali Aike volcanics (mainly whole-rock analyses) are currently available (Mercer, 1976; Linares and Gonzalez, 1990; Meglioli, 1992; Singer et al., 1997; Corbella, 1999b). The ages obtained span the time interval from 3.78 to 0.17 Ma, with the oldest rocks cropping out in the western sector of the volcanic field.

In this study, the PAVF succession is subdivided into three units (Fig. 2) listed here from oldest to youngest:

U1 — plateau-like basal lavas

U2 — dissected old cones, tuff rings, maars and associated lava flows

U3 — well preserved, young (possibly up to protohistoric) scoria cones and associated lava flows with little eolian soil cover.

The distribution of lava flows and monogenetic apparata was studied through satellite images, stereo pairs and geological field survey. A total of 468 volcanic apparata were recognized: 442 belong to the U2 unit, and 26 to the U3 unit. Overall, the surface covered by the volcanics is approximately 4500 km^2. The U1, U2 and U3 units occupy 83, 15, and 2% of the surface of the whole volcanic field, respectively. The average thickness of the volcanic pile, evaluated on several sections, is about 100 m. Assuming a duration of the volcanic activity of 3.8 m.y., an effusion rate in the order of 10^{-4} km^3 yr^{-1} is obtained. This value is considerably lower (at least two orders of magnitude) than those typical for melt production rates above mantle plumes (White, 1993).

Orientations of elongated structural features have been analyzed with results presented in Figs. 2 and 3. Sixty-four alignments of three or more cones considered as coeval and belonging to U2, and five alignments of U3 cones, were identified. The azimuths of the basal elongation of single cones were determined for 154 U2 and seven U3 cones. The results are displayed in the rose diagrams of Fig. 3a and b. The azimuth distribution of both cone alignment and elongation clearly shows NW–SE and ENE–WSW prevailing trends; a minor NS trend is also observed for the distribution of cone elongation.

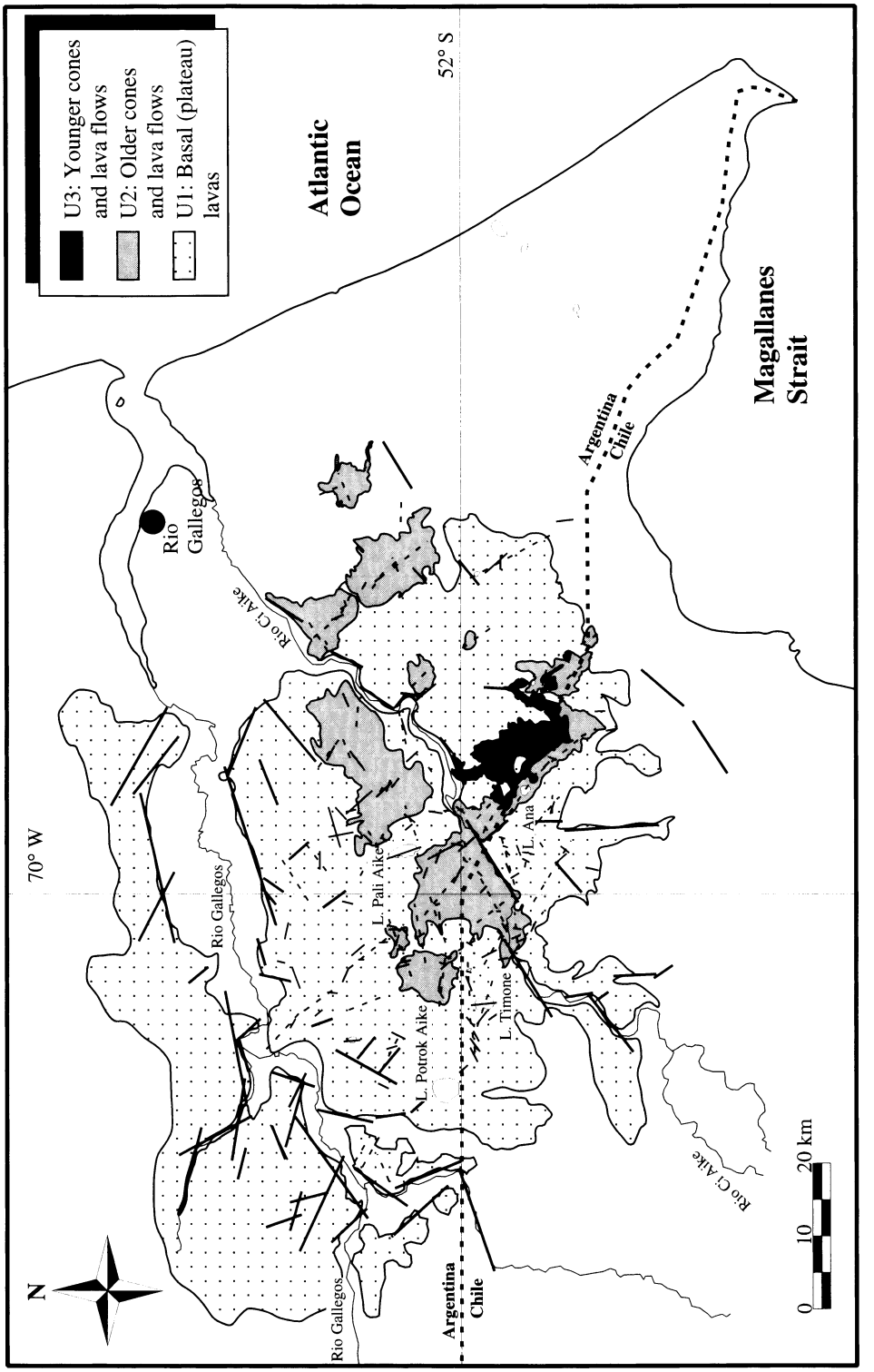

Fig. 2. Geological sketch map of the Pali Aike Volcanic Field. Thick solid lines: lineations, dashed lines: cone alignments, thin solid lines: cone elongations.

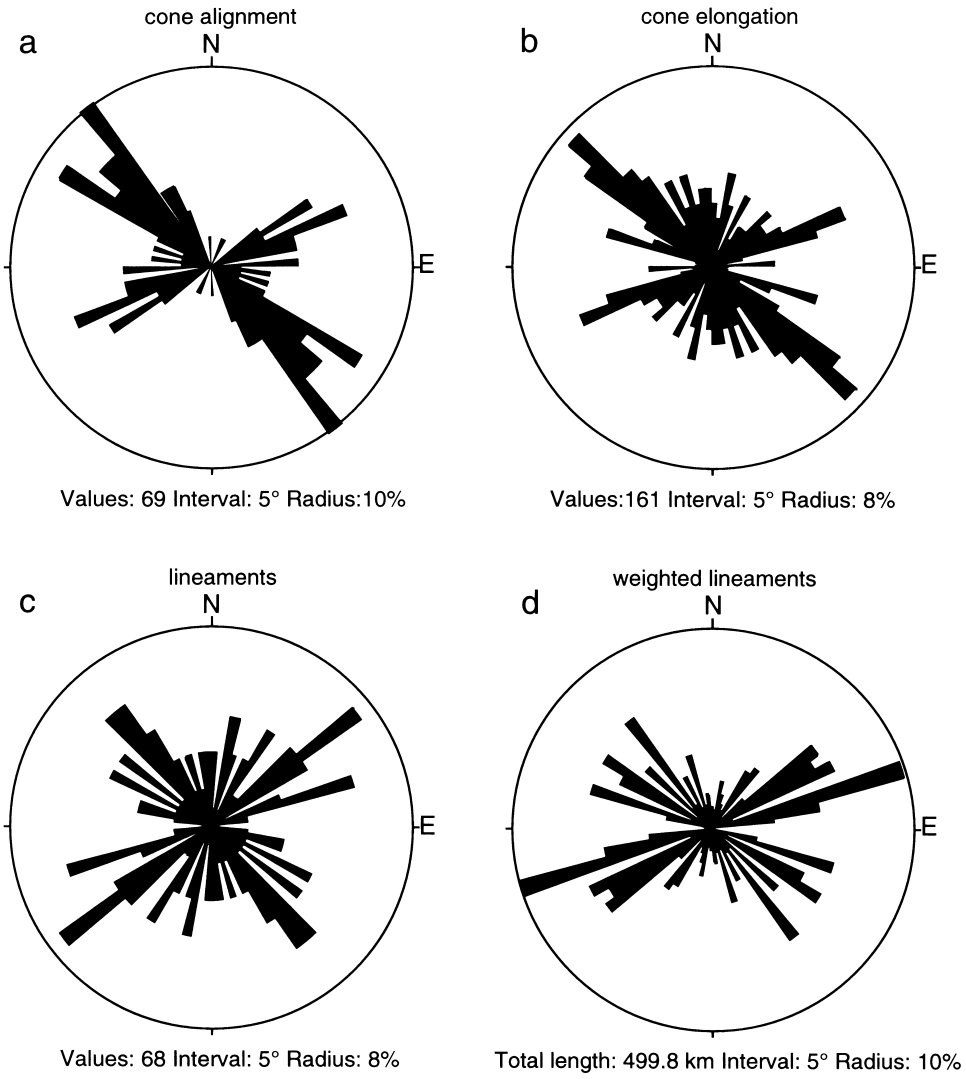

Fig. 3. Distribution analysis of structural features. (a) rose diagram of alignments of more than three coeval cones; (b) rose diagram of cone elongation; (c) rose diagram for the main lineations recognized by satellite image analysis; (d) frequency distribution of length-weighted lineations.

Structural analysis of satellite images allowed determination of the direction and length of the most prominent lineations affecting the areal morphology of the volcanic field. Lengths range between 2 and 23 km (average 7.6 km), with the ENE–WSW concentration dominant over the NW–SE one (Fig. 3c and d). The ENE–WSW alignment parallels the main trend of the still active Magallanes Strait Rift System described by Diraison et al. (1997). Moreover, the NW–SE direction, outlined mainly by the elongation and alignment of cones, matches the trend of the Mesozoic Patagonian Austral Rift (Corbella et al., 1996). The occurrence of the same structural trends for the monogenetic structures of U2 and U3, as well as for the linear features recognized mainly in the basal plateau-like lavas (U1), suggests that the stress field controlling the volcanic activity did not

change significantly during emission of the whole Pali Aike volcanic pile.

4. Analytical methods

Whole-rock chemical analyses (major and trace elements) were performed at the Dipartimento di Scienze della Terra, Università di Pisa. Major elements plus V, Cr, Co and Ni were determined by XRF on pressed powder pellets using an automated Philips PW1480 X-ray spectrometer with a full matrix correction procedure after Franzini et al. (1975) and Leoni and Saitta (1976). MgO and Na_2O were determined by AAS, FeO by titration and L.O.I. gravimetrically. The concentrations of Sc, Rb, Sr, Y, Zr, Nb, Cs, Ba, REE, Hf, Ta, Th and U were determined by ICP-MS (Fisons PQII+ STE).

Mineral chemistry data were obtained by means of a JEOL JXA-8600 electron microprobe (Centro di Studio per la Minerogenesi e la Geochimica Applicata, C.N.R., Florence) operating at 15 kV and 10 nA and with a matrix correction procedure after Bence and Albee (1968).

Sr and Nd isotopic analyses were carried out using a Finnigan MAT 262V multicollector mass spectrometer (Istituto di Geocronologia e Geochimica Isotopica, C.N.R., Pisa) and conventional ion exchange methods for Sr and Nd separations. Measured $^{87}Sr/^{86}Sr$ ratios were normalized to $^{86}Sr/^{88}Sr = 0.1194$; $^{143}Nd/^{144}Nd$ ratios were normalized to $^{146}Nd/^{144}Nd = 0.7219$. During the collection of isotopic data for this study, replicate measurements of NIST SRM 987 ($SrCO_3$) and La Jolla standards gave values of 0.710166 ± 12 (2σ ext) for $^{87}Sr/^{86}Sr$ and 0.511852 ± 14 (2σ ext) for $^{143}Nd/^{144}Nd$. The measured $^{87}Sr/^{86}Sr$ and $^{143}Nd/^{144}Nd$ ratios for the samples of this study were normalized to a value of $^{87}Sr/^{86}Sr = 0.710250e$ and $^{143}Nd/^{144}Nd = 0.511850$ for NIST SRM 987 and La Jolla, respectively.

5. Classification, petrography and mineral chemistry

Over 70 rock samples representing all three PAVF volcanic units were collected during austral summers 96/97 and 97/98 (GPS coordinates of sample sites are available from the first author). The majority of recovered rocks do not contain microscopically detectable alteration materials except for the occasional slight oxidation of olivine phenocrysts forming iddingsitic products.

The volcanic rocks from the PAVF have an alkaline affinity and mainly belong to a sodic series (Table 1). In the TAS diagram (Fig. 4), they plot in the basalt and basanite (normative ol 14–29%) fields, defining a rough negative correlation between silica and alkalis. Two samples fall in the trachybasalt field of the TAS diagram, close to the boundary with the basalt field; however, these rocks are characterized by a high MgO content ($\sim$10 wt.%) and Mg# ($\sim$67). Thus, in the following sections, they will be grouped with the alkali basalt samples. It is worth noting that most of the volcanics from old plateaus (U1) and from the youngest centers (U3) are less alkaline than are the intermediate-aged cones of U2 (Fig. 4). In particular, nine out of 22 samples belonging to U1 are hy-normative and are here classified as olivine basalts.

Ultramafic xenoliths of mantle origin are found in high abundance within some lava flows and tuff-ring deposits (Skewes and Stern, 1979; Stern et al., 1986, 1989, 1999; Kempton et al., 1998a,b). They consist predominantly of spinel, garnet, and spinel+garnet lherzolites and harzburgites, Ti-augite megacrysts and subordinate wehrlites and pyroxenites. The lavas occasionally contain xenocrysts of olivine and minor pyroxene and spinel derived from disrupted ultramafic xenoliths; olivine xenocrysts are distinguished from phenocrysts by their tabular shape, kink banding and slightly larger size (up to 5 mm). Chemically, olivine xenocrysts display higher NiO/CaO ratios (>5 for xenocrysts and <1.5 for phenocrysts) and higher Fo content (Fig. 5). Samples contaminated by more than 1% mantle olivine xenocrysts, identified in the diagrams with filled symbols, are omitted in subsequent discussions of geochemical data.

Sampled lavas are porphyritic–glomeroporphyritic to subaphyric (P.I. 5–20) containing ubiquitous olivine phenocrysts, generally bearing chrome-spinel inclusions. Other phenocrysts

Table 1
Representative major- and trace-element analyses and Sr–Nd isotope data of volcanic rocks from the Pali Aike Volcanic Field[a]

Sample	PA-121	PA-129	PA-240	PA-242	PA-243	PA-205	PA-210[b]	PA-213	PA-217	PA-222	PA-230	PA-234[b]	PA-237	AOB-1	PA-118	PA-224
Unit	U1	U1	U1	U1	U1	U2	U2	U2	U2	U2	U2	U2	U2	U3	U3	U3
Latitude	52°04′03″S	52°03′03″S	51°50′27″S	51°50′27″S	51°50′27″S	52°03′27″S	52°01′13″S	52°00′04″S	52°03′00″S	52°02′57″S	51°57′28″S	51°59′43″S	51°57′30″S	52°04′51″S	52°05′06″S	52°07′49″S
Longitude	70°04′12″W	70°03′14″W	70°29′58″W	70°29′58″W	70°29′58″W	69°48′36″W	70°12′17″W	70°12′50″W	70°03′13″W	70°01′13″W	70°14′10″W	70°10′20″W	70°02′16″W	69°46′18″W	69°43′38″W	69°33′10″W
Classification	ol bas	ol bas	basanite	alk bas	ol bas	alk bas	basanite	alk bas	alk bas	basanite	alk bas	basanite	alk bas	alk bas	alk bas	alk bas
SiO_2 (wt%)	48.15	48.19	43.80	45.45	48.14	45.95	43.39	46.52	46.64	43.84	46.69	43.20	46.09	47.14	46.57	47.40
TiO_2	2.97	3.32	3.32	2.46	2.75	2.80	2.77	2.60	3.39	3.81	2.42	2.46	2.76	2.89	2.78	2.84
Al_2O_3	14.29	14.48	12.24	13.21	13.96	11.71	10.14	12.78	11.30	11.44	13.68	11.48	12.79	13.56	13.11	12.38
Fe_2O_3	3.50	4.11	3.79	2.33	3.98	10.04	4.78	3.90	5.68	6.97	2.57	4.99	2.52	3.01	2.88	7.99
FeO	6.80	6.64	8.18	8.45	6.51	1.39	6.77	7.22	7.52	5.87	7.57	6.18	7.88	8.79	8.77	3.38
MnO	0.15	0.15	0.16	0.17	0.15	0.17	0.17	0.16	0.18	0.17	0.15	0.16	0.15	0.16	0.16	0.16
MgO	7.97	6.36	11.83	11.00	8.36	12.23	14.99	10.87	8.06	10.07	10.34	16.04	11.06	9.91	10.95	11.29
CaO	9.73	9.84	9.34	10.24	9.98	9.37	10.49	10.00	11.57	11.26	10.04	9.41	10.72	9.38	9.27	8.97
Na_2O	3.24	3.14	3.53	3.53	2.98	3.10	3.49	3.33	3.39	3.27	3.68	3.45	3.36	3.03	3.00	3.07
K_2O	1.39	1.65	1.88	1.20	1.34	1.35	1.25	1.17	1.28	1.94	1.47	1.19	1.22	1.21	1.26	1.26
P_2O_5	1.00	0.81	0.90	0.75	0.90	0.66	0.75	0.64	0.54	0.77	0.82	0.75	0.94	0.46	0.51	0.58
LOI	0.81	1.31	1.03	1.22	0.95	1.23	1.00	0.81	0.44	0.57	0.58	0.70	0.51	0.47	0.74	0.69
Mg#	61.8	55.4	67.4	67.8	62.6	70.4	73.3	67.2	56.3	62.7	67.9	75.3	68.8	63.6	66.1	68.4
ne-hy	-4.2	-6.1	11.8	8.6	-2.1	4.9	14.0	5.6	6.9	12.5	8.0	13.1	6.9	2.0	2.2	1.5
Sc (ppm)	21	20	19	21	25	19	14	19	22	22	21	19	20	22	24	24
V	256	267	251	227	244	236	239	228	265	293	218	230	231	241	248	262
Cr	185	194	360	314	290	365	476	274	203	293	212	550	277	261	362	346
Co	44	43	56	51	44	53	56	50	49	53	47	60	48	51	57	53
Ni	98	72	287	239	146	338	429	247	158	178	189	495	203	210	262	278
Rb	22.6	32.8	30.4	18.5	25.0	24.5	31.6	21.6	24.7	34.6	27.1	23.7	19.4	24.5	21.8	24.2
Sr	839	778	939	934	832	684	819	727	730	876	805	741	813	586	640	635
	28.4	29.5	29.0	25.0	27.8	23.1	22.1	24.1	25.5	27.8	26.4	22.5	24.1	24.2	24.0	25.0
Zr	214	234	299	191	219	202	200	165	176	264	188	193	165	181	198	211
Nb	55	55	70	52	50	52	68	48	50	68	59	55	51	39	43	45
Cs	0.38	0.61	0.51	0.39	0.34	0.39	0.77	0.31	0.44	0.56	0.92	0.35	0.28	0.41	0.31	0.40
Ba	488	584	505	419	431	523	598	433	477	599	521	483	532	335	362	388
La	42	40	50	36	40	35	49	35	38	44	42	40	46	26	28	31
Ce	84	81	104	73	82	75	93	70	72	87	81	82	87	54	59	63
Pr	10.5	10.3	13.0	9.0	10.5	8.9	10.8	8.6	8.9	11.2	9.7	9.8	10.4	7.0	7.5	8.2
Nd	44	43	54	38	44	37	43	36	37	47	40	40	42	30	33	35
Sm	9.4	9.3	11.3	8.2	9.4	7.9	8.6	7.9	8.2	9.9	8.6	8.3	8.8	7.0	7.5	7.8
Eu	3.05	2.88	3.50	2.55	3.01	2.51	2.61	2.50	2.62	3.16	2.67	2.69	2.80	2.29	2.37	2.54
Gd	8.4	8.7	9.8	7.4	8.2	7.5	7.3	7.2	7.4	9.1	7.8	7.4	7.5	6.7	6.8	7.4
Tb	1.17	1.23	1.35	1.02	1.13	0.98	0.97	1.01	1.04	1.23	1.09	1.03	1.04	0.99	0.98	1.04
Dy	6.1	6.1	6.5	5.4	5.8	5.0	4.8	5.1	5.4	6.1	5.5	5.1	5.1	5.0	5.1	5.2
Ho	1.04	1.08	1.15	0.93	0.99	0.86	0.83	0.92	0.94	1.06	1.02	0.86	0.93	0.91	0.87	0.97
Er	2.44	2.57	2.41	2.25	2.31	1.96	1.85	2.01	2.23	2.34	2.26	2.01	2.06	2.02	2.14	2.06
Tm	0.32	0.35	0.32	0.27	0.30	0.28	0.25	0.30	0.31	0.32	0.33	0.26	0.28	0.29	0.28	0.31
Yb	1.78	1.86	1.62	1.63	1.69	1.46	1.36	1.55	1.66	1.65	1.69	1.34	1.51	1.59	1.52	1.66
Lu	0.24	0.26	0.21	0.20	0.22	0.20	0.17	0.21	0.22	0.23	0.24	0.17	0.20	0.20	0.20	0.24
Hf	4.8	5.3	6.6	4.5	5.1	4.4	4.6	3.8	4.0	6.0	4.3	4.3	3.8	4.3	4.6	5.0
Ta	2.86	3.06	4.18	2.83	2.74	2.85	3.60	2.49	2.47	3.89	2.86	3.11	2.42	2.30	2.46	2.71
Th	5.0	5.4	5.6	4.2	4.5	4.1	6.4	4.2	4.7	5.2	5.6	4.8	6.0	3.3	3.2	3.4
U	1.52	1.45	1.70	0.93	0.92	1.16	1.62	1.15	1.27	1.52	1.34	1.32	1.39	0.98	0.95	1.03
$^{87}Sr/^{86}Sr$		0.703391	0.703248					0.703206					0.703166			0.703326
$^{143}Nd/^{144}Nd$			0.512900					0.512938					0.512944			0.512896

[a] ol bas: olivine basalt; alk bas: alkali basalt; subalk bas: subalkaline basalt. Mg# = $Mg/(Mg+Fe^{2+})\times 100$ assuming Fe_2O_3/FeO (wt%) = 0.15. ne-hy = wt% normative nepheline minus wt% normative hyperstene.

[b] Samples contaminated by more than 1% by weight of xenocrystic olivine.

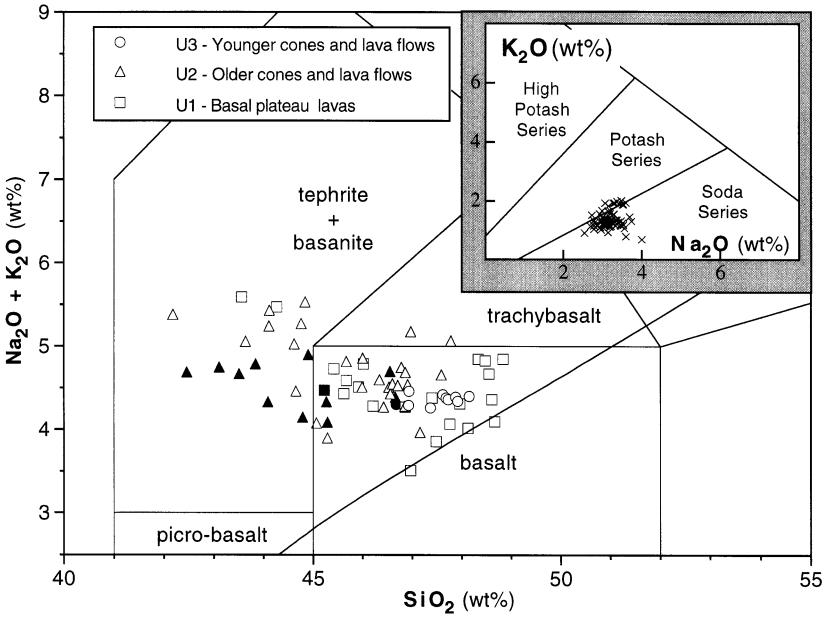

Fig. 4. Total alkali vs. silica classification diagram for Pali Aike rocks. Black symbols indicate samples contaminated by more than 1% of xenocrystic mantle olivine. The boundary line between alkaline and subalkaline rocks of Irvine and Baragar (1971) is also plotted. Inset: K_2O vs. Na_2O diagram, reporting the boundary lines between high potash, potash and soda series after Middlemost (1975).

include clinopyroxene and, less frequently, plagioclase: about 37% of the samples have olivine as the unique phenocryst phase, 49% have olivine + diopside, and only 14% have olivine + diopside + plagioclase. Scoriae are similar to lavas, except for their lower porphyricity and more glass-rich groundmass. Alkali and olivine basalts and basanites exhibit very similar petrographic features, and were thus classified purely on chemical bases. However, plagioclase phenocrysts were found exclusively in the basalts, and quite large clinopyroxene phenocrysts (up to 3 mm) occur commonly in the olivine basalts.

The whole range of olivine phenocryst composition (Table 2) is Fo 78–88. Fe-rich rims affected by incipient iddingsite replacement were also analyzed. The olivine–liquid geothermometer of Leeman and Scheidegger (1977) was applied to samples with low porphyricity and containing only olivine as a phenocryst phase. It was assumed that olivine phenocryst cores were in equilibrium with a silicate liquid whose composition coincided with that of the whole rock (the Fe_2O_3/FeO ratio of the latter was normalized to 0.15). The resulting temperatures vary between 1200 and 1290°C.

Clinopyroxene phenocrysts are diopsidic (rarely augitic) in composition (Table 3); their sizes are generally smaller than coexisting olivine. Frequently, clinopyroxene phenocrysts occur as glomerophyric aggregates.

Plagioclase phenocrysts are characterized by well-developed normal zoning and andesine-labradorite compositions (Table 4).

Groundmass textures are generally microcrystalline and, more rarely, cryptocrystalline or glassy. Textures are commonly intergranular or intersertal, hyalopilitic for glassy types. The ubiquitous assemblage olivine, brownish diopside-augite, plagioclase, alkali feldspar (sanidine and anorthoclase) and Ti-magnetite characterize all studied samples. More silica undersaturated samples also contain interstitial nepheline, whilst olivine basalts carry ilmenite together with the Ti-magnetite (Table 5). Six samples containing groundmass magnetite–ilmenite pairs were studied for oxygen barometry and geothermometry estimates.

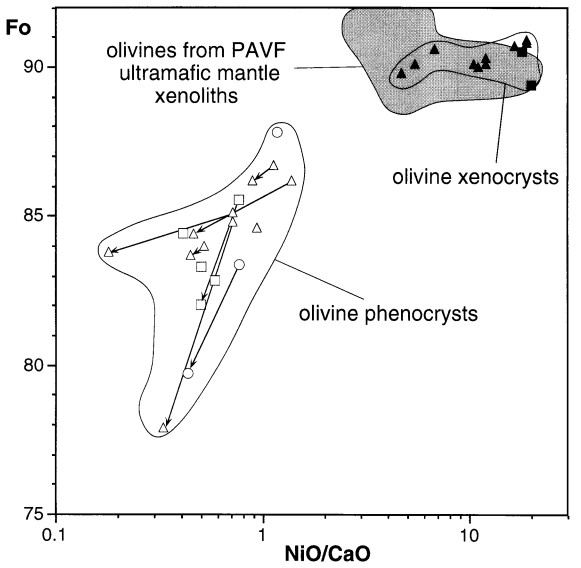

Fig. 5. Fo content vs. NiO/CaO wt.% ratios for olivine crystals from the Pali Aike Volcanic Field. Olivine crystals originating from the disruption of ultramafic mantle xenoliths (black symbols) are characterized by significantly higher Fo and NiO/CaO ratios with respect to olivine phenocrysts crystallizing from Pali Aike magmas. Arrows join cores to rims of phenocrysts. The gray area encloses olivines from peridotite and pyroxenite xenoliths hosted inside Pali Aike volcanics (data from Kempton et al., 1998a). Symbols as in Fig. 4.

According to the Ghiorso and Sack (1991) formulation, the groundmass of these six samples equilibrated at temperatures ranging from 870 to 1090°C with oxygen fugacity ranging from −1.7 to −0.3 QFM log units (Table 5). The lower temperature values are ascribed to subsolidus re-equilibration of magnetite–ilmenite pairs.

6. Geochemical and Sr–Nd isotope results

6.1. Chemistry

PAVF volcanics are quite primitive in composition, as testified to by Mg#s ranging from 55 to 70 (average = 66 ± 3, 1 S.D.), MgO contents from 6.4 to 13.0 wt.% (average = 10.6 ± 1.3 wt.%) and CaO from 8.8 to 11.8 wt.% (average = 9.8 ± 0.7 wt.%). Major elements showing the highest variability are P_2O_5, K_2O, MgO and TiO_2. The latter is present in all samples at relatively high levels (average = 3.0 ± 0.4 wt.%) (Table 1).

The primitive nature of the PAVF rocks is confirmed by the high concentrations of Ni (average = 220 ± 78 ppm) and Cr (average = 313 ± 75 ppm). Ti/V ratios vary between 62 and 88 (average = 70 ± 6). These values are within the typical range (50–100) for intra-plate basaltic alkaline lavas and well above the range for MORB (20–50), back-arc basin (10–50) and island arc (10–20) basic lavas (Shervais, 1982).

The content of Cr and, to a lesser extent, that of Co decrease sharply with decreasing Ni, while Sc and V concentrations remain almost constant (Fig. 6). As Ni and Co are favorably partitioned into olivine, Cr into spinel and Sc and V into clinopyroxene, the variations of these elements in

Table 2
Selected analyses of olivine[a]

Sample	PA-108 ph. core	PA-108 ph. rim	PA-222 ph. core	PA-222 ph. rim	PA-125 ph. core	PA-125 ph. rim	PA-127 xenocryst	AOB-1 grm	PA-213 grm
SiO_2	40.09	40.11	40.43	40.27	40.30	39.80	40.75	37.84	37.70
FeO	12.85	13.29	13.28	14.80	13.92	17.14	9.23	25.33	27.01
MnO	0.13	0.15	0.17	0.21	0.18	0.26	0.12	0.33	0.52
NiO	0.28	0.24	0.29	0.19	0.20	0.18	0.44	0.12	<d.l.
MgO	46.89	46.68	46.65	44.97	46.20	43.90	49.93	35.99	35.71
CaO	0.25	0.27	0.21	0.41	0.26	0.36	0.05	1.21	0.47
Sum	100.49	100.74	101.03	100.85	101.06	101.64	100.52	100.82	101.41
Fo%	86.7	86.2	86.2	84.4	85.5	82.0	90.6	71.7	70.2
NiO/CaO	1.1	0.9	1.4	0.5	0.8	0.5	8.8	0.1	–

[a] ph.: phenocryst; grm: groundmass; <d.l.: below detection limit.

Table 3
Selected analyses of clinopyroxene

Sample	PA-108 ph. core	PA-108 ph. rim	PA-126 ph. core	PA-126 ph. rim	PA-222 ph. core	PA-222 ph. rim	PA-230 ph. core	PA-230 ph. rim	PA-222 grm	PA-245 grm
SiO_2	48.78	45.5	50.56	45.91	51.28	49.94	51.02	50.16	45.35	46.85
TiO_2	2.17	3.78	1.11	3.16	1.27	1.78	1.38	1.69	4.29	3.55
Al_2O_3	3.22	5.99	2.92	6.61	2.39	3.53	3.64	3.92	6.92	6.26
Cr_2O_3	0.32	0.28	0.33	<d.l.	0.61	0.80	0.71	<d.l.	0.16	0.11
FeO	6.32	7.3	6.53	8.31	4.62	5.00	4.78	6.69	7.34	8.92
MgO	15.15	12.95	15.64	12.67	15.64	15.03	14.78	14.32	12.48	12.35
CaO	23.41	23.11	22.07	21.69	23.22	23.29	22.85	22.78	22.63	21.23
Na_2O	0.34	0.56	0.41	0.58	0.34	0.37	0.42	0.37	0.5	0.59
Sum	99.71	99.47	99.57	98.93	99.37	99.74	99.58	99.93	99.67	99.86
Wo%	47.4	49.4	45.1	47.4	47.8	48.4	48.5	47.5	49.5	46.8
En%	42.6	38.5	44.5	38.5	44.8	43.5	43.6	41.6	38.0	37.9
Fs%	10.0	12.2	10.4	14.2	7.4	8.1	7.9	10.9	12.5	15.3

Table 4
Selected analyses of feldspar

Sample	AOB-1 ph. core	AOB-1 ph. rim	PA-126 ph. core	PA-126 ph. rim	PA-230 ph. core	PA-230 ph. rim	PA-111 grm	PA-213 grm	PA-109 grm	PA-230 grm
SiO_2	52.58	55.33	51.55	52.50	54.19	55.49	58.49	55.60	63.42	65.56
Al_2O_3	28.58	26.88	29.94	29.49	28.75	27.54	25.28	26.00	21.78	19.11
Fe_2O_3	0.70	0.78	0.61	0.71	0.61	0.42	0.3785	1.79	0.36	0.37
CaO	11.43	9.26	12.61	11.91	11.67	9.78	6.01	9.01	2.63	0.35
Na_2O	4.82	5.72	4.17	4.67	4.92	5.52	7.58	6.17	7.59	4.60
K_2O	0.48	0.80	0.26	0.30	0.40	0.56	0.43	0.47	3.69	9.99
sum	98.59	98.77	99.14	99.58	100.54	99.31	98.17	99.04	99.47	99.98
An%	55.5	45.5	61.6	57.5	55.4	47.9	29.7	44.5	12.7	1.7
Ab%	41.7	49.9	36.9	40.8	42.3	48.9	67.8	52.9	66.2	40.5
Or%	2.7	4.6	1.5	1.7	2.3	3.3	2.5	2.7	21.2	57.8

Table 5
Selected analyses of groundmass magnetite–ilmenite pairs[a]

Sample Phase	PA-109 mt	PA-109 ilm	PA-111 mt	PA-111 ilm	PA-114 mt	PA-114 ilm	PA-125 mt	PA-125 ilm	PA-126 mt	PA-126 ilm	PA-245 mt	PA-245 ilm
TiO_2	28.03	50.16	24.75	47.92	26.37	51.03	27.87	51.36	29.71	50.73	29.75	49.08
Al_2O_3	1.23	<d.l.	2.19	1.75	1.92	<d.l.	1.55	<d.l.	0.87	<d.l.	0.48	1.51
Cr_2O_3	<d.l.	<d.l.	0.19	<d.l.	0.28	<d.l.	<d.l.	<d.l.	<d.l.	<d.l.	<d.l.	<d.l.
FeO_{tot}	66.69	46.53	66.69	43.59	64.85	42.56	66.94	45.73	63.42	44.57	62.38	42.86
MnO	0.56	0.80	0.50	0.85	0.62	0.75	0.61	0.73	0.76	0.97	0.70	0.67
MgO	2.40	1.48	1.82	2.57	4.51	3.75	1.22	1.73	2.53	2.54	1.72	2.08
CaO	<d.l.	0.20	0.15	0.42	0.14	0.46	0.12	0.17	0.11	0.28	0.47	0.61
Sum	98.91	99.17	96.29	97.10	98.69	98.55	98.31	99.72	97.40	99.09	95.50	96.80
T (°C)	976		1029		867		874		1093		1062	
ΔQFM	−0.8		−0.3		−0.9		−1.7		−1.0		−1.4	

[a] Temperature and oxygen fugacity calculated according to the Fe–Ti oxide geothermometer of Ghiorso and Sack (1991). mt: Ti-magnetite; ilm: ilmenite.

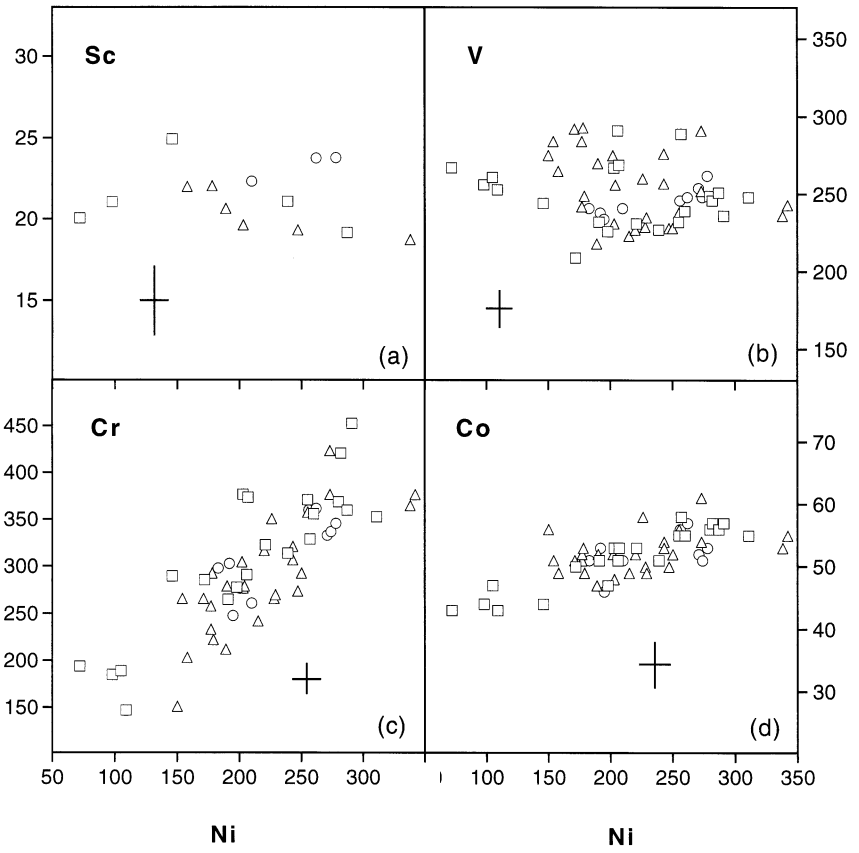

Fig. 6. Sc (a), V (b), Cr (c), Co (d) vs. Ni (ppm) diagrams for Pali Aike volcanics not contaminated by mantle xenolith-derived material. Crosses indicate typical uncertainties (1 S.D.). Symbols as Fig. 4.

the studied lavas strongly suggest that fractionation of olivine, plus included Cr-spinel, played a dominant role in the differentiation of the PAVF volcanics.

Chondrite-normalized REE patterns are significantly LREE-enriched ($La_N = 108–212$, $Yb_N = 9.1–11.5$) and almost rectilinear (Fig. 7). The $(La/Yb)_N$ ratio, used as a measure of LREE/HREE fractionation, varies for the whole data set from 10.9 to 21.0. Samples from U1 and U2 show a tendency toward a higher $(La/Yb)_N$ (average = 16.9) with respect to the recent cones of U3 (average = 12.1). LREE/HREE fractionation increases with increasing concentration of incompatible elements, suggesting a variation in the degree of melting during the genesis of PAVF magmas.

Primordial mantle-normalized patterns (Fig. 8) show the typical humped distribution characterizing basalts from intraplate continental and oceanic settings (e.g. Sun and McDonough, 1989). The patterns reach their maximum height at the 'twin' elements Nb and Ta and tend to converge at the heaviest REE. Negative anomalies of Hf and K are quite evident. Ratios between the most hygromagmatophile elements vary within the analytical error (e.g. Ba/Nb, La/Nb) or nearly so (e.g. Ba/La, Ba/Th, Th/U); a notable exception is the ratio Rb/Cs (relative standard deviation, RSD = 21%), whose variability is certainly due to the high mobility of these alkaline elements during even slight weathering and to the reduced precision in the determination of low amounts of Cs (0.3–0.9 ppm).

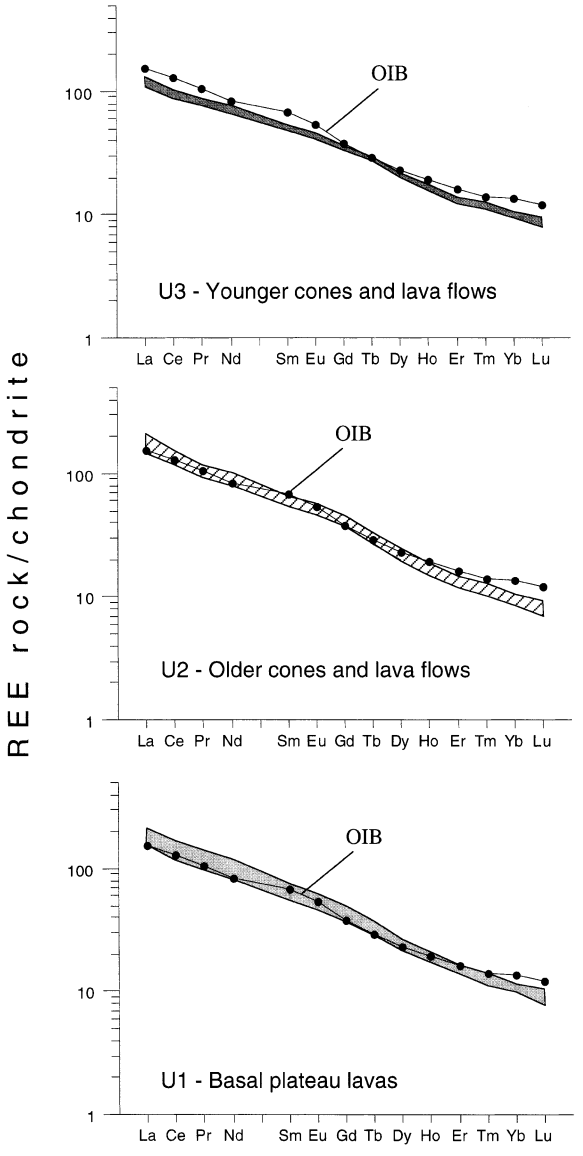

Fig. 7. Chondrite-normalized REE patterns for Pali Aike volcanics subdivided into U1, U2 and U3 stratigraphic units. The REE pattern of the average OIB of Sun and McDonough (1989) is also plotted for comparative purposes. Normalizing values after McDonough and Sun (1995).

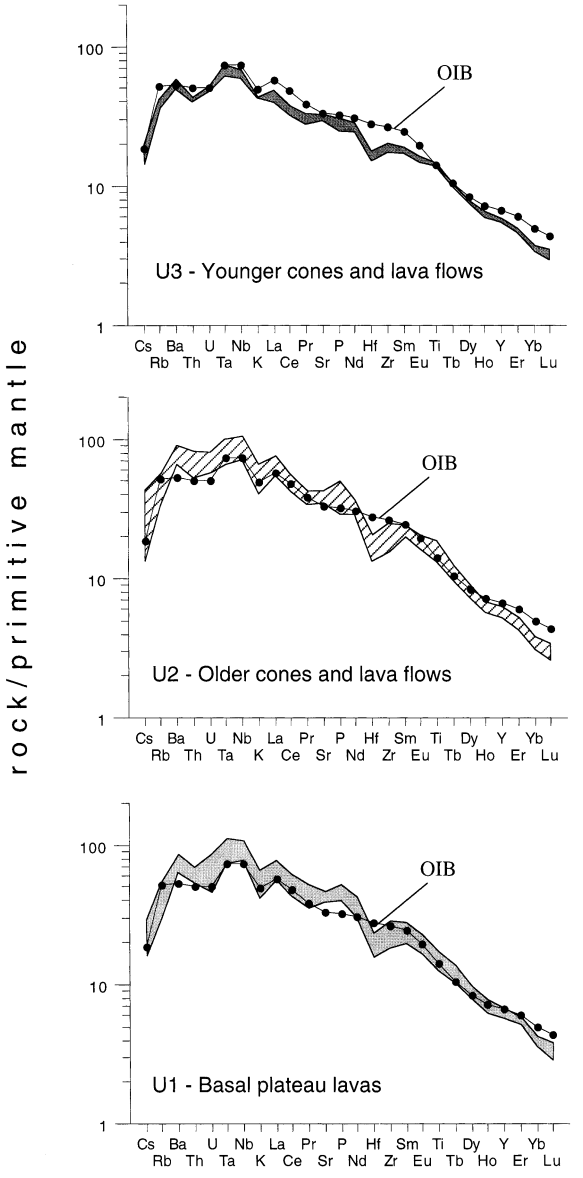

Fig. 8. Primordial mantle-normalized incompatible element patterns for Pali Aike volcanics subdivided into U1, U2 and U3 stratigraphic units. The pattern of the average OIB of Sun and McDonough (1989) is also plotted for comparative purposes. Normalizing values after McDonough and Sun (1995).

6.2. *Sr–Nd isotopes*

Sr and Nd isotope compositions determined for five samples ($^{87}Sr/^{86}Sr = 0.70317–0.70339$, $^{143}Nd/^{144}Nd = 0.51290–0.51294$) fall in the depleted quadrant of the plane $^{143}Nd/^{144}Nd$–$^{87}Sr/^{86}Sr$, in a position commonly occupied by many continental and ocean island basalts (Fig. 9). Our values closely match those reported by Stern et al. (1990) and confirm that, in terms of Sr–Nd isotopes, Pali Aike basaltic rocks are the most depleted of all

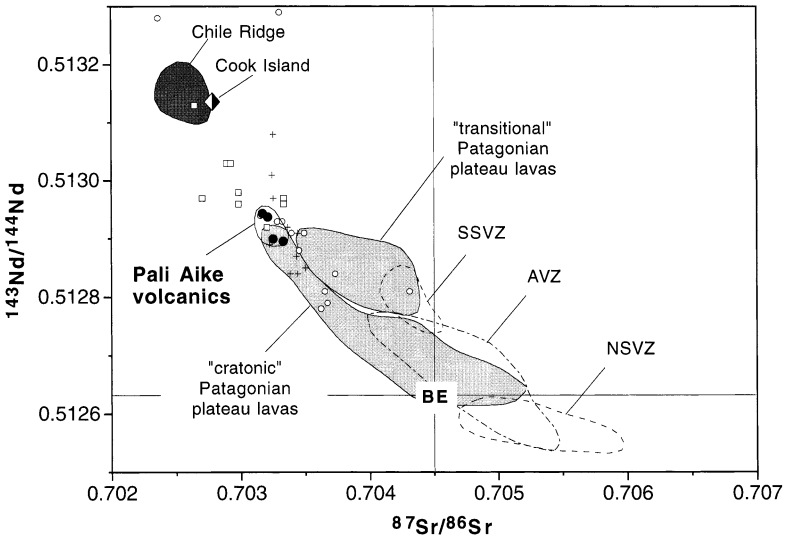

Fig. 9. $^{143}Nd/^{144}Nd$ vs. $^{87}Sr/^{86}Sr$ diagram for the Pali Aike Volcanic Field (filled circles) and for other Cenozoic southern South America volcanic rocks. Data: Patagonian Plateau lavas: Stern et al. (1990), Gorring et al. (1997); Chile Ridge: Klein and Karsten (1995), Bach et al. (1996); Cook Island: Stern and Kilian (1996); Northern South Volcanic Zone (NSVZ), Southern South Volcanic Zone (SSVZ) and Austral Volcanic Zone (AVZ) of the Andes: Futa and Stern (1988), Stern and Kilian (1996). Data for the Pali Aike mantle xenoliths are also reported: circles, spinel peridotites (whole rocks and clinopyroxene); squares, garnet-bearing peridotites (whole rocks and clinopyroxene); crosses, modally metasomatized peridotites (whole rocks, clinopyroxene, phlogopite and amphibole). Data from Kempton et al. (1998b) and Stern et al. (1999). BE: bulk earth.

the Neogene Patagonian Plateau lavas of southernmost South America. Unlike the lavas, the Pali Aike mantle xenoliths distribute over a wide area in the Sr–Nd isotope diagram. Considerably depleted ($^{87}Sr/^{86}Sr < 0.7025$, $^{143}Nd/^{144}Nd > 0.5132$) and reasonably enriched ($^{87}Sr/^{86}Sr = 0.7043$, $^{143}Nd/^{144}Nd = 0.5128$) Sr–Nd isotope compositions for the xenoliths are indicative of an isotopically heterogeneous lithospheric mantle below the Pali Aike region (Kempton et al., 1998b; Stern et al., 1999).

On the basis of chemistry, Sr–Nd–Pb–O isotopes and geologic position, Stern et al. (1990) divided the Pliocene–Quaternary Patagonian plateau basalts into the 'cratonic' and 'transitional' groups. The first group includes lavas erupted far to the east of the Andean arc and characterized by OIB-type trace-element and isotopic features. In contrast, the second group crop out within areas affected by Cenozoic Andean volcanism and have chemical and isotopic characteristics intermediate between the 'cratonic' basalts and the Andean arc basalts. In this sense, the PAVF products fully belong to the 'cratonic' group.

7. Petrogenesis of PAVF magmas

Silicate liquids in equilibrium with olivine Fo_{90} (a reasonable composition for common mantle peridotites, Ormerod et al., 1991) at mantle pressures, should have Mg#s of $\sim 76 \pm 1$, significantly higher than Mg#s observed for PAVF whole rocks (omitting those contaminated by mantle xenoliths). This suggests that none of the magmas that erupted, except those carrying ultramafic xenoliths, reached the surface without some fractionation of femic mineral phases. In a previous section, we showed that the distribution of Ni, Cr, V, Co and Sc in the studied lavas is strongly indicative that only olivine (plus minor spinel to account for the Ni–Cr covariation) acted as a fractionating phase during the differentiation of PAVF primary magmas.

Accordingly, to estimate the possible composition of primary magmas, equilibrium olivine was continuously added back into whole rock compositions until they were in equilibrium with mantle olivine Fo_{90}. These calculations included: (1) the fractional crystallization equation of Pearce (1978); (2) a constant Fe_2O_3/FeO wt.% ratio of 0.15 for starting compositions; (3) a constant $Kd^{ol\text{-}liq}$ of 0.30 (Roeder and Emslie, 1970). The calculations were performed only for the PAVF rocks closest to a primary magma composition, arbitrarily defined as those having Mg# > 68. For these samples, the required amount of olivine added back in varied between 5 and 10 wt.%. The estimated primary magmas (selected anhydrous compositions are listed in Table 6) are ne-normative or slightly hy-normative, and have an average MgO content of 14.3 wt.%. Estimated PAVF primary magmas are very close in composition to those experimentally obtained by anhydrous melting of natural peridotites at pressures of 2.5–3.0 GPa and 1450–1475°C by Hirose and Kushiro (1993). A similar range of P–T melting conditions (1.9–2.9 GPa; 1420–1470°C) was found by applying the empirical relationships proposed by Albarede (1992). Under these thermobaric conditions, both garnet and spinel can be the aluminous stable phase in the mantle (McKenzie and O'Nions, 1991). However, the high LREE/HREE fractionation, the almost rectilinear shape of the REE patterns, and the covariation between LREE/HREE ratios and highly incompatible element concentrations are all strongly indicative of residual garnet in the mantle source of PAVF magmas. The common occurrence of garnet-bearing ultramafic mantle xenoliths inside the volcanic rocks from PAVF confirms this conclusion.

8. Geodynamic significance of PAVF

The geochemical study of the volcanic products occurring at the PAVF clearly shows that, notwithstanding the proximity of the volcanic field to an active destructive plate margin, their mantle source is completely lacking in the typical geochemical signatures of subduction-related components (Skewes and Stern, 1979; Stern et al., 1990; Corbella, 1999a). Indeed, the primitive and minimally variable erupted lavas bear strong OIB-like character, testified to by low Ba/Nb(Ta), La/Nb(Ta) and high Ti/V ratios. Isotope compositions of Sr and Nd also indicate an isotopically depleted OIB-type source. Petrological and geochemical data point to magma generation in the garnet stability field that is at depths in excess of 80 km (McKenzie and O'Nions, 1991).

PAVF is located in the proximity of a destructive

Table 6
Selected major-element compositions of calculated primary magmas

Sample	PA-113	PA-242	PA-247	PA-124	PA-205	PA-237	PA-250	PA-224
Unit	U1	U1	U1	U2	U2	U2	U2	U3
SiO_2 (wt.%)	46.5	45.6	45.2	46.7	46.6	46.0	44.4	47.4
TiO_2	2.6	2.3	3.1	2.5	2.7	2.6	2.6	2.6
Al_2O_3	12.0	12.2	11.8	12.5	11.4	12.0	12.9	11.5
Fe_2O_3	1.4	1.3	1.3	1.3	1.3	1.3	1.3	1.3
FeO	9.9	9.5	9.5	9.6	9.4	9.1	9.5	9.5
MnO	0.1	0.2	0.1	0.1	0.2	0.1	0.2	0.1
MgO	15.0	14.4	14.3	14.5	14.3	13.8	14.5	14.5
CaO	8.8	9.5	9.6	8.7	9.1	10.0	9.5	8.4
Na_2O	2.4	3.3	3.2	2.6	3.0	3.1	3.4	2.9
K_2O	0.9	1.1	1.3	1.1	1.3	1.1	0.8	1.2
P_2O_5	0.5	0.7	0.6	0.6	0.6	0.9	1.0	0.5
ne-hy	-1.4	7.6	8.0	0.8	4.4	6.2	7.8	1.1
Added ol%[a]	8.9	9.7	6.3	9.1	5.1	7.7	8.1	8.8

[a] Added ol%: weight per cent of equilibrium olivine added to obtain a melt in equilibrium with olivine Fo_{90}.

plate margin characterized by a long history of subduction. In particular, after the closure of the 'Rocas Verdes' back-arc basin in early Cretaceous time (Dalziel, 1981), the eastern Pacific and South American Plates were dominated by pure convergence. Such a geodynamic situation should have created a supra-slab mantle contaminated by slab-derived fluids and/or melts, and possibly also modified by the extraction of calc-alkaline melts. The existence of a pristine asthenospheric source below the PAVF requires a mechanism able to efficiently replace the slab-modified mantle with an unmodified mantle.

The PAVF grew in a region between the on-land linear projections of the Desolación and Madre de Dios oceanic fracture zones (Fig. 1). These zones bounded a segment of the Chile Ridge that, according to plate reconstruction models (Cande and Leslie, 1986), collided with the Chile Trench at 14 Ma. This geodynamic setting produced a slab-free region (slab window) beneath the overriding southernmost South America. Assuming a convergence rate between the Nazca and South American Plates of 9–10 cm yr^{-1} over the last 25 m.y. and a subduction angle of 30° (Turcotte and Schubert, 1982; Cande and Leslie, 1986), the trailing edge of the Nazca Plate crossed the present position of Pali Aike 4–5 m.y. after ridge-trench collision. Thus, the passage of the slab window predates the onset of the magmatic activity at PAVF by 4–6 m.y. We hypothesize that during this time-span, the supra-slab mantle was largely replaced by pristine asthenosphere that flowed through the slab window to become the mantle source of the Pali Aike basaltic magmas (Fig. 10).

The delay between volcanic activity and slab window passage under the PAVF contrasts with the situation observed for the Patagonian Plateau lavas north of 49.5° S where the passage of the trailing edge of the Nazca Plate was followed shortly (<1 m.y.) by the eruption of extensive subalkaline basalts, named 'main plateau lavas' by Gorring et al. (1997). The same authors hypothesized that the absence of mid-Miocene plateau magmatism south of 49.5° S was caused by differences in the chemical and physical characteristics of the subslab asthenosphere, asthenospheric wedge and/or continental lithosphere, that could have been colder, drier and less fertile with respect to the region to the north.

We consider that the main factor determining the different time distribution of slab window magmatism occurring at the PAVF could be ascribed to the unique geotectonic setting that characterizes the tip of South America. The relative motion between the South American and Antarctic Plates produced since Cretaceous a counterclockwise crustal rotation of the South America tip, leading to a 90° bend in the Andean Cordillera, referred to as the Patagonian orocline (e.g. Cunningham, 1993). The rotation produced a fragmentation of the southernmost Andes into crustal blocks bounded by left-lateral strike slip faults. As the rotation proceeded, regions formerly subjected to pure convergence experienced a sequence of tectonic regimes from transpressional to pure strike-slip and finally transtensional. This sequence of crustal deformation progressively migrated northward (Cunningham, 1993). From about 30 to 8 Ma, the relative motion between South American and Antarctic Plates was accommodated by NW–SE-directed seafloor spreading that formed the Scotia Plate (Barker and Dalziel, 1983; Cunningham et al., 1995). Between 8 and 6 Ma, this NE-trending ridge ceased to spread, and a new E–W seafloor spreading started to the east (Barker and Burrell, 1977; Pelayo and Wiens, 1989; Barker et al., 1991). As a consequence of the change in spreading direction in the Scotia Plate, all the relative movements between South America and Antarctica were accommodated by two transform plate boundaries: the South and North Scotia Ridges. The prolongation of the North Scotia Ridge into the South American conti-

Fig. 10. Cartoon showing the slab-window opening beneath southern South American Plate since 14 Ma. PA, present position of Pali Aike Volcanic Field. Gray areas: surface projection of the slab-free region; black areas: slab-window related Patagonian Plateau lavas; gray arrows: asthenospheric mantle flows; black arrows: plate motion relative to a fixed South America; thick black lines: segments of the Chile Ridge; thin dashed lines: oceanic fracture zones.

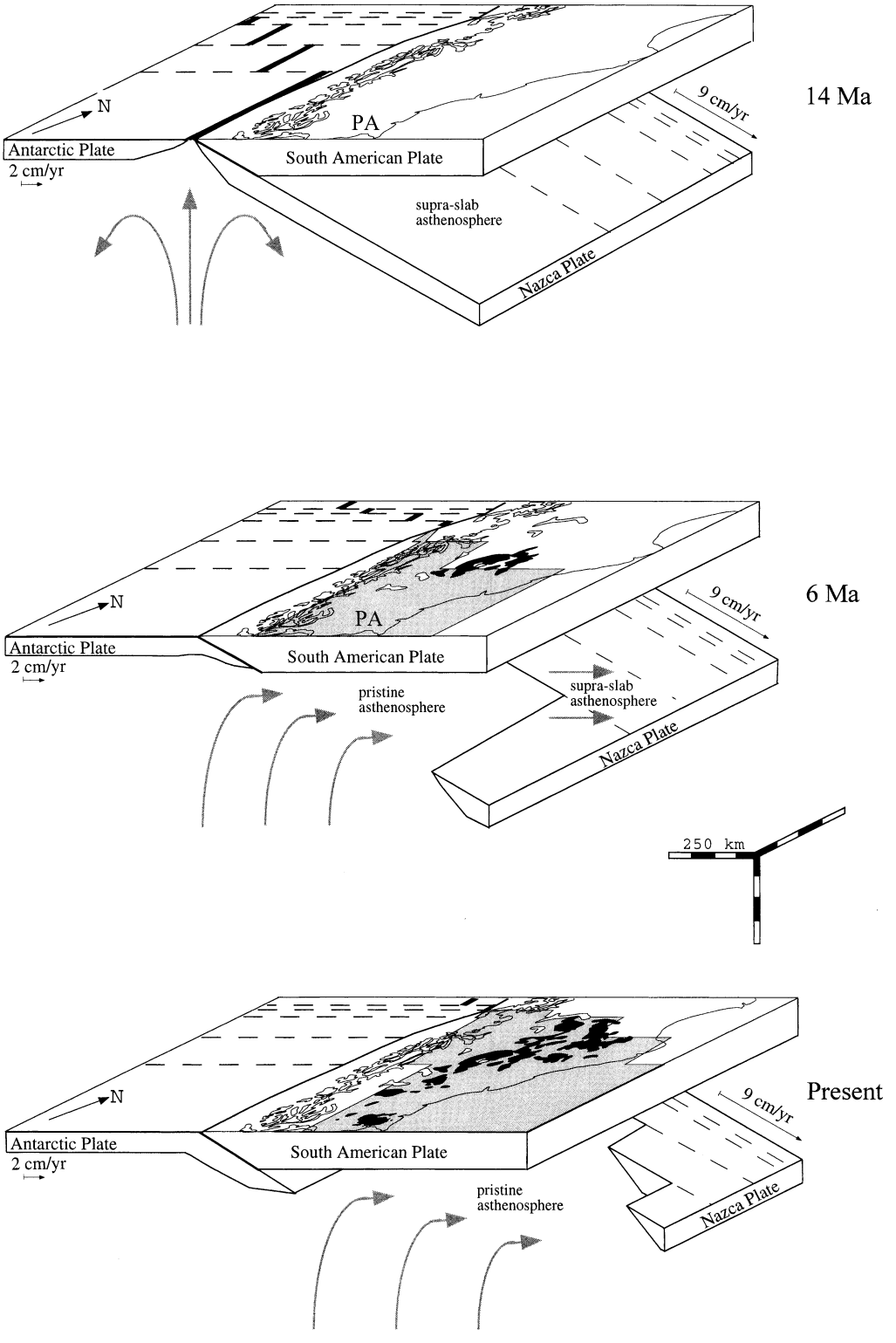
14 Ma
N
PA
Antarctic Plate
2 cm/yr
South American Plate
9 cm/yr
supra-slab
asthenosphere
Nazca Plate
6 Ma
N
PA
Antarctic Plate
2 cm/yr
South American Plate
9 cm/yr
pristine
asthenosphere
supra-slab
asthenosphere
Nazca Plate
250 km
Present
N
Antarctic Plate
2 cm/yr
South American Plate
9 cm/yr
pristine
asthenosphere
Nazca Plate

nent is represented by the Magallanes Fault System (Klepeis, 1994). Fault-slip data, morphotectonic analyses, as well as earthquake focal mechanisms, point to a sinistral, transtensional kinematics along the Magallanes Fault (Pelayo and Wiens, 1989; Diraison et al., 1997; Klepeis and Austin, 1997). The ENE-trending Neogene Magallanes Strait rift system (Diraison et al., 1997), located in the foreland where the PAVF developed, was considered as a consequence of the transtensional tectonics along the South America–Scotia plate boundary.

We speculate that an extensional tectonic regime, favorable to the ascent of the magmas, was present in the Pali Aike area only after 8–6 Ma, when a plate reorganization event induced a significant extensional component in the left-lateral transform boundary between the South American and Scotia Plates. The collected structural data indicate that the PAVF volcanism was essentially controlled by ENE- and NW-trending structures. The former could be interpreted as an expression of the Magallanes Strait Rift System; the latter could be interpreted as P fractures (Sylvester, 1988) reactivating the NW-trending Mesozoic faults that bounded the Austral Patagonian Rift (Corbella et al., 1996).

9. Summary and conclusions

- The PAVF is the youngest and southernmost of the Cenozoic Patagonian basaltic plateaus. It covers about 4500 km^2 north of the Magallanes fault system and 200 km east of the Andean Cordillera.
- More than 80% of the erupted products consist of an extensive succession of plateau-like basaltic lavas. The remaining volcanics are constituted by more than 450 monogenetic structures represented by maars, tuff-rings, scoria and spatter cones, and by associated lava flows. The whole volcanic succession is divided into three units: a basal plateau-like unit (U1), a unit of old partially eroded cones (U2), and a unit of young, well-preserved cones and lava flows (U3). The volcanic activity spans from about 3.8 Ma to Recent. An effusion rate in the order of 10^{-4} km^3 yr^{-1} has been roughly estimated.
- The elongation of cones, the alignment of coeval cones and the directions of prominent lineations reveal that all volcanic activity at the PAVF was strongly controlled by ENE- and NW-trending tectonic structures.
- The erupted products are alkali and olivine basalts and basanites. They are characterized by highly primitive composition; 88% of the studied samples have MgO > 9 wt.%, Mg# > 61, Ni > 150 ppm and Cr > 200 ppm. The near primary composition of the PAVF magmas is supported by the occurrence of ultramafic mantle xenoliths, sometimes remarkably garnet-bearing.
- Trace-element distribution is relatively homogeneous and reveals a typical within-plate OIB-like signature. REE patterns are almost rectilinear and display LREE-enrichment and high LREE/HREE ratios. Sr–Nd isotope compositions are close to MORB values and are the most depleted among the whole set of Cenozoic Patagonian plateau lavas.
- Geochemical data indicate a fertile garnet-bearing asthenospheric source for the PAVF magmatism. Following the collision of the Chile Ridge with the Chile Trench at 14 Ma, sub-slab asthenosphere flowed up through the slab window below this sector of South America.
- The 4–6 m.y. delay between the passage of the trailing edge of the Nazca Plate beneath the PAVF area and the subsequent volcanic activity is attributed to the peculiar geotectonic position of the volcanic field. The rise of the PAVF magmas became possible following the onset of transtensional tectonics in the Pali Aike region. We speculate that this occurred only after 8–6 Ma as a consequence of a prominent change in the kinematics of the South America–Scotia plate boundary.

Acknowledgements

D.S. Westerman and R. Mazzuoli are acknowledged for their useful comments and suggestions to the first version of the manuscript. Many thanks

to S. Tonarini for her assistance during Sr–Nd isotope analyses. The Chilean Empresa Nacional de Petroleo (ENAP) is greatly acknowledged for its valuable logistic support during field work. Many thanks also to O. Gonzalez-Ferran and C. Meister for stimulating discussions during field work. The final version of the manuscript benefited by the thorough reviews of P.D. Kempton, D.J. Thorkelson and an anonymous referee. This research was supported by the Italian National Antarctic Research Program (PNRA) and by MURST-ITALY.

References

Albarede, F., 1992. How deep do common basaltic magmas form and differentiate. J. Geophys. Res. 97, 10997–11009.

Bach, W., Erzinger, J., Dosso, L., Bollinger, C., Bougault, H., Etoubleau, J., Sauerwein, J., 1996. Unusually large Nb–Ta depletions in North Chile Ridge basalts at 36°50′ to 38°56′S, major element, trace element and isotopic data. Earth Planet. Sci. Lett. 142, 223–240.

Barker, P.F., Burrell, J., 1977. The opening of Drake Passage. Mar. Geol. 25, 15–34.

Barker, P.F., Dalziel, I.W.D., 1983. Progress in geodynamics of the Scotia Arc region. In: Cabre, R. (Ed.), Geodynamics of the eastern Pacific region, Caribbean and Scotia Arcs. Geodyn. Ser. 9. AGU, Washington, DC, pp. 137–170.

Barker, P.F., Dalziel, I.W.D., Storey, B.C., 1991. Tectonic development of the Scotia Arc region. In: Tingey, R. (Ed.), Geology of Antarctica. Oxford University Press, New York, pp. 215–248.

Bence, A.E., Albee, A.L., 1968. Empirical correction factors for the electron microanalyses of silicates and oxides. J. Geol. 76, 382–483.

Bevier, M.L., 1983. Implications of chemical and isotopic composition for petrogenesis of Chilcotim Group Basalts, British Columbia. J. Petrol. 24, 207–226.

Cande, S.C., Leslie, R.B., 1986. Late Cenozoic tectonics of the Southern Chile Trench. J. Geophys. Res. 91, 471–496.

Clapperton, C.M., 1983. The glaciation of the Andes. Quat. Sci. Rev. 2, 83–155.

Corbella, H., Chelotti, L., Pomposiello, C., 1996. Neotectonica del rift Jurasico austral en Pali Aike, Patagonia Extrandina, Santa Cruz, Argentina. In: XIII Congreso Geológico Argentino y III Congreso de Exploracion de Hidrocarburos, Actas, II, 383–393.

Corbella, H., 1999a. Quimismo de las volcanitas de Pali Aike, Patagonia Austral In: XIV Congreso Geológico Argentino, Actas, II, 269–272.

Corbella, H., 1999b. Dataciones radimétricas en Pali Aike, Patagonia Austral In: XIV Congreso Geológico Argentino, Actas, II, 265–268.

Cunningham, W.D., 1993. Strike-slip faults in the southernmost Andes and the development of the Patagonian Orocline. Tectonics 12, 169–186.

Cunningham, W.D., Dalziel, I.W.D., Lee, T.I., Lawver, L.A., 1995. Southernmost South America–Antarctic Peninsula relative plate motions since 84 Ma: Implications for the tectonic evolution of the Scotia Arc region. J. Geophys. Res. 100, 8257–8266.

Dalziel, I.W.D., 1981. Back-arc extension in the southern Andes: a review and critical reappraisal. Phil. Trans. R. Soc. London 300, 319–335.

Dickinson, W.R., Snyder, W.S., 1979. Geometry of subducted slabs related to the San Andreas transform. J. Geol. 87, 609–627.

Diraison, M., Coppold, P.R., Gapais, D., Rossello, E.A., 1997. Magellan Strait: part of a Neogene rift system. Geology 25 (8), 703–706.

Forsythe, R.D., Nelson, E.P., Carr, M.J., Kaeding, M.E, Herve, M., Mpodozis, C., Soffia, J.M., Harambour, S., 1986. Pliocene near-trench magmatism in southern Chile: A possible manifestation of ridge collision. Geology 14, 23–27.

Forsythe, R.D., Prior, D., 1992. Cenozoic continental geology of South America and its relations to the evolution of the Chile Triple Junction. In: Behrmann, J.H., Lewis, S.D., Musgrave, R.J. et al., (Eds.), Proc. ODP Init. Rep. Vol. 141, 23–31.

Franzini, M., Leoni, L., Saitta, M., 1975. Revisione di una metodologia analitica per fluorescenza-X, basata sulla correzione degli effetti di matrice. Rend. Soc. It. Mineral. Petrol. 31, 365–378.

Furlong, K.P., Chapman, D.S., Alfeld, P.W., 1982. Thermal modeling of the geometry of subduction with implications for the tectonics of the overriding plate. J. Geophys. Res. 87, 1786–1802.

Futa, K., Stern, C.R., 1988. Sr and Nd isotopic and trace element composition of Quaternary volcanic centers of southern Andes. Earth Planet. Sci. Lett. 88, 253–263.

Ghiorso, M.S., Sack, R.O., 1991. Fe–Ti oxide geothermometry. Thermodynamic formulation and the estimation of intensive variables in silicic magmas. Contrib. Mineral. Petrol. 108, 485–510.

Gorring, M.L., Kay, S.M., Zeitler, P.K., Ramos, V.A., Rubiolo, D., Fernandez, M.I., Panza, J.L., 1997. Neogene Patagonian plateau lavas: Continental magmas associated with ridge collision at the Chile Triple Junction. Tectonics 16 (1), 1–17.

Gripp, A.E., Gordon, R.G., 1990. Current plate velocities relative to the hot spots incorporating the NUVEL-1 global plate motion model. Geophys. Res. Lett. 17, 1109–1112.

Hirose, K., Kushiro, I., 1993. Partial melting of dry peridotites at high pressures: Determination of compositions of melts segregated from peridotite using aggregates of diamond. Earth Planet. Sci. Lett. 114, 477–489.

Hole, M.J., Rogers, G., Saunders, A.D., Storey, M., 1991. The relationship between alkalic volcanism and slab window formation. Geology 19, 657–660.

Hole, M.J., Saunders, A.D., Rogers, G., Sykes, M.A., 1995.

The relationship between alkaline magmatism, lithospheric extension and slab window formation along continental destructive plate margins. In: Smellie, J.L. (Ed.), Volcanism Associated with Extension at Consuming Plate Margins. Geol. Soc. Spec. Publ. 81, 265–285.

Irvine, T.N., Baragar, W.R.A., 1971. A guide to the chemical classification of the common volcanic rocks. Can. J. Earth Sci. 8, 523–548.

Johnson, C.M., O'Neill, J.R., 1984. Triple junction magmatism: a geochemical study of Neogene volcanic rocks in western California. Earth Planet. Sci. Lett. 71, 241–262.

Johnston, S.T., Thorkelson, D.J., 1997. Cocos-Nazca slab window beneath Central America. Earth Planet. Sci. Lett. 146, 465–474.

Kempton, P.D., Lopez-Escobar, L., Hawkesworth, C.J., Pearson, G., Ware, A.J., 1998a. Spinel ± Garnet lherzolite Xenoliths from Pali Aike, Part 1. Petrography, Mineral Chemistry and Geothermobarometry, in press.

Kempton, P.D., Hawkesworth, C.J., Lopez-Escobar, L., Ware, A.J., 1998b. In: Spinel ± Garnet Lherzolite Xenoliths from Pali Aike, Part 2. Trace Element and Isotopic Evidence Bearing on the Evolution of Litospheric Mantle Beneath Southern Patagonia, in press.

Klein, E.M., Karsten, J.L., 1995. Ocean-ridge basalts with convergent-margin geochemical affinities from the Chile Ridge. Nature 374, 52–57.

Klepeis, K.A., 1994. The Magallanes and Deseado fault zones, major segments of South American–Scotia transform plate boundary in southernmost South America, Tierra del Fuego. J. Geophys. Res. 99, 22001–22014.

Klepeis, K.A., Austin Jr., J.A., 1997. Contrasting styles of superposed deformation in the southernmost Andes. Tectonics 16, 755–776.

Leeman, W.P., Scheidegger, K.F., 1977. Olivine/liquid distribution coefficients and a test for crystal–liquid equilibrium. Earth Planet. Sci. Lett. 35, 247–257.

Leoni, L., Saitta, M., 1976. X-ray fluorescence analysis of 29 trace elements in rock and mineral standards. Rend. Soc. It. Mineral. Petrol. 32, 497–510.

Linares, E., Gonzalez, R.R., 1990. Catàlogo de edades radimètricas de la Repùblica Argentina 1957–1987. In: Asociaciòn Geològica Argentina Publicaciones Especiales Serie B 19, 628 pp.

McDonough, W.F., Sun, S.S., 1995. The composition of the Earth. Chem. Geol. 120, 223–253.

McKenzie, D., O'Nions, R.K., 1991. Partial melt distributions from inversion of rare earth element concentrations. J. Petrol. 32, 1021–1091.

Meglioli, A., 1992. Glacial geology and geochronology of southernmost Patagonia and Tierra del Fuego, Argentina and Chile. Ph.D. dissertation, Leigh University, Bethlehem, PA.

Mercer, J.H., 1976. Glacial history of southernmost South America. Quat. Res. 6, 125–166.

Middlemost, E.A.K., 1975. The basalt clan. Earth Sci. Rev. 11, 337–364.

Ormerod, D.S., Rogers, N.W., Hawkesworth, C.J., 1991. Melting in the lithospheric mantle: Inverse modelling of alkali-olivine basalts from the Big Pine Volcanic Field, California. Contrib. Mineral. Petrol. 108, 305–317.

Pearce, T.H., 1978. Partial melt distributions from inversion of rare earth element concentrations. Nature 276, 771–774.

Pelayo, A.M., Wiens, D.A., 1989. Seismotectonics and relative plate motion in the Scotia Sea region. J. Geophys. Res. 94, 7293–7320.

Ramos, V.A., 1989. Foothills structure in Northern Magallanes Basin, Argentina. AAPG Bull. 73, 887–903.

Ramos, V.A., Kay, S.M., 1992. Southern Patagonian plateau basalts and deformation: backarc testimony of ridge collisions. Tectonophysics 205, 261–282.

Roeder, P.L., Emslie, R.F., 1970. Olivine–liquid equilibrium. Contrib. Mineral. Petrol. 29, 275–289.

Saunders, A.D., Rogers, G., Marriner, G.F., Terrell, D.J., Verma, S.P., 1987. Geochemistry of Cenozoic volcanic rocks, Baja California, Mexico: Implications for the petrogenesis of post-subduction magmas. J. Volcanol. Geotherm. Res. 32, 223–245.

Shervais, J.W., 1982. Ti–V plots and the petrogenesis of modern and ophiolitic lavas. Earth Planet. Sci. Lett. 59, 101–118.

Singer, B.S., Ton-That, T., Vincze, T., Rabassa, J., Roig, C., Brunstad, K., 1997. Timescale of late Cenozoic climate change in the southern hemisphere from $^{40}Ar/^{39}Ar$ dating of Patagonia lavas. Terra Abs., Eur. Union Geosci. 9 (9), 65–66.

Skewes, M.A., Stern, C.R., 1979. Petrology and geochemistry of alkali basalts and ultramafic inclusions from the Palei-Aike volcanic field in southern Chile and the origin of the Patagonian plateau lavas. J. Volcanol. Geotherm. Res. 6, 3–25.

Stern, C.R., Futa, K., Saul, S., Skewes, M.A., 1986. Ultramafic xenoliths from the Pali-Aike basalts: implications for the nature and evolution of the subcontinental lithosphere below southern South America. In: Smith, C.B. (Ed.), Fourth International Kimberlite Conference. Abstracts, Geological Society of Australia Vol. 16, 343–345.

Stern, C.R., Saul, S., Skewes, M.A., Futa, K., 1989. Garnet peridotite xenoliths from the Pali Aike basalts of southernmost South America. Geol. Soc. Austral. Spec. Publ. 14, 735–744.

Stern, C.R., Frey, F.A., Futa, K., Zartman, R.E., Peng, Z., Kyser, T.K., 1990. Trace-element and Sr, Nd, Pb and O isotopic composition of Pliocene and Quaternary alkali basalt of the Patagonian Plateau lavas of southernmost South America. Contrib. Mineral. Petrol. 104, 294–308.

Stern, C.R., Kilian, R., 1996. Role of the subducted slab, mantle wedge and continental crust in the generation of adakites from the Andean Austral Volcanic Zone. Contrib. Mineral. Petrol. 123, 263–281.

Stern, C.R., Kilian, R., Olker, B., Hauri, E.H., Kyser, T.K., 1999. Evidence from mantle xenoliths for relatively thin (<100 km) continental lithosphere below the Phanerozoic crust of southernmost South America. Lithos 48, 217–235.

Sun, S.S., McDonough, W.F., 1989. Chemical and isotopic systematics of oceanic basalts, implications for mantle composition and processes. In: Saunders, A.D., Norry, M.J.

(Eds.), Magmatism in the Ocean Basins. Geol. Soc. London, Spec. Publ. 42., 313–345.

Sylvester, A.G., 1988. Strike-slip faults. Geol. Soc. Am. Bull. 100, 1666–1703.

Thorkelson, D.J., 1996. Subducing of diverging plates and the principles of slab window formation. Tectonophysics 255, 47–63.

Toksöz, M.N., Bird, P., 1977. Formation and evolution of marginal basins and continental plateaus. In: Talwani, M., Pitman III, W.C. (Eds.), Island Arcs Deep Sea Trenches and Back-arc Basins, Maurice Ewing Series Vol. I, 379–393.

Turcotte, D.L., Schubert, G., 1982. Geodynamics: Applications of Continuum Physics to Geological Problems. Wiley, New York. 450 pp.

Urien, C.M., Zambrano, J.J., Yrigoyen, M.R., 1995. Petroleum basins of southern South America, an overview. In: Tankard, A.J., Soruco, R.S., Welsink, H.J. (Eds.), Petroleum Basins of South America. AAPG Memoir 62, 63–77.

White, R.S., 1993. Melt production rates in mantle plumes. In: Cox, K.G., McKenzie, D.P., White, R.S. (Eds.), Philos. Trans. R. Soc. London 342, 137–153.

Winslow, M.A., 1982. The structural evolution of the Magallanes Basin and neotectonics in the southernmost Andes. In: Craddock, C. (Ed.), Antarc. Geosci., 143–154.